Research Square

Preprints are preliminary reports that have not undergone peer review.
They should not be considered conclusive, used to inform clinical practice,
or referenced by the media as validated information.

Stonehenge's geometry and counts recover interior dimensions and select Cygnus near 3000 BCE

Lucas Giovani Ribeiro

coin26@mail.com

Independent Researcher

Marcos André Simonssini

Independent Researcher

Article

Keywords:

Posted Date: November 19th, 2026

DOI: https://doi.org/10.21203/rs.3.rs-11569495/v1

License: This work is licensed under a Creative Commons Attribution 4.0 International License.
Read Full License

Additional Declarations: No competing interests reported.

Stonehenge's geometry and counts recover interior dimensions and select Cygnus near 3000 BCE

Lucas Giovani Ribeiro * and Marcos André Simonssini

Independent Researcher, Uruana de Minas, Minas Gerais 38630-000, Brazil

Lucas Giovani Ribeiro: coin26@mail.com; ORCID 0009-0002-1417-0062

Marcos André Simonssini: thecygnuscode@gmail.com; ORCID 0009-0000-9076-6410

* Correspondence: coin26@mail.com

Abstract

We recover four interior dimensions of Stonehenge from exterior geometry using one calibration and four elementary operations, with 2.02% root-mean-square error. The assigned lengths minimize each dimensional error within an explicit operation library. Architectural counts specify angular intervals whose stellar matches evolve under precession and proper motion. At a fixed quarter degree per count, Cygnus ranks first among 19,939 brightness-defined five-star fields near 2965 BCE, with a runner-up error 2.20 times larger. The search excludes archaeological dates; restricting it to the later sarsen phase raises the minimum error 5.33-fold. Reference-radius calibration also selects Cygnus. A retrospective Woodhenge extension gives an optimum near 2609 BCE: only one of 5,832 arithmetic targets combines error below 0.2° with a minimum in its published construction interval. These dimensional relations connect heritage reconstructions through coupled geometry; the celestial references connect count models with independently dated building phases.

1. Introduction

Stonehenge's successive building phases pose a problem of design continuity. The monument in Wiltshire, southern England, developed from an earthwork enclosure around 3000 BCE into arrangements of large stones and later hole circuits [1–3]. Its four Station positions define a peripheral rectangle, and the Aubrey Holes form a ring of 56 early settings. The mean Station short side is 33.435 m, close to the approximately 33 m outer diameter of the central sarsen circle [1,2,4]. Transferring that exterior length to the interior is a simple construction. A rule connecting several dimensions specifies what a shared design would preserve across rebuilding.

We recover four interior dimensions from the Station–Aubrey frame using one exterior calibration. Copying a side, halving another, subtracting a side from the diagonal and constructing an inradius generate lengths assigned to the sarsen circle, Z and Y circuits and trilithon span, with 2.02% relative RMS error. Four separately described features thus become outputs of one frame. The equations specify how changes in the exterior propagate into the interior and couple the interior dimensions to one another. Alternative operations, feature weights and measurement changes can therefore be compared within the same reconstruction.

The Station rectangle has long been studied through Pythagorean proportions, solar and lunar directions, horizon phenomena and latitude [5–8]. Excavation, provenance and landscape research establish the material sequence for evaluating these proposals [9–20]; traceable sources and feature boundaries define the reconstruction inputs [21].

Precession gives the architectural count model a temporal reference. Ecliptic coordinates describe stars relative to Earth's orbital plane; the longitude differences and latitudes used here vary slowly in the stated frame. Right ascension measures position around Earth's rotation axis. Precession changes that axis relative to the stars and hence the intervals between their meridian transits, expressed as rotation angles. Comparing a fixed angular target with these changing intervals locates a best-fit reference epoch. Stellar proper motion is included, and section 2.3 specifies the coordinate conventions.

Cygnus contains the Northern Cross, formed by Deneb, Sadr, Albireo, Aljanah and Fawaris, five bright stars along the Milky Way. We compare the count-derived target with five-star fields generated by apparent brightness and spherical geometry, assign their roles geometrically and search over 10,000 years. At the fixed angular calibration, Cygnus ranks first among 19,939 fields near 2965 BCE. Archaeological chronology enters afterward: the same model fits the initial enclosure more closely than the later sarsen phase. Woodhenge supplies a second count target, whose optimum near 2609 BCE falls in its later timber-construction interval. Section 2.5 distinguishes the prior Stonehenge target from the date-informed selection at Woodhenge.

The target has an antecedent in the authors' Cygnus work. The January 2026 account assigns roles to 16, 28, 34 and 62 [22]; the Calanais material deposited publicly on 26 August 2026 (Zenodo 22103786) records W=(28,72,16) and a minimum near 2965 BCE. The present study establishes how Stonehenge's counts generate that target and compares its stellar fit with alternative fields. Section 2.5 states the information order. S9 contains extended architectural analyses; S10 develops a subsequent four-position extension and its controls. S11 reports the Woodhenge comparison and its complete arithmetic target census.

2. Methods

2.1. Architectural inputs and exterior calibration

The inventory is A=56 Aubrey positions, B=30 outer sarsen uprights, C=10 trilithon uprights and D=4 Station positions. Sarsens are the large silcrete stones; each trilithon comprises two uprights supporting a lintel. The inventory is reconstructed across building phases and includes absent settings. Table 1 identifies the source, boundary and precision class of every dimensional input. The primary Station values are Atkinson's reported centre-to-centre distances [23, pp. 50–52], explicitly reproduced in MacKie's appendix [24, p. 107]. Stations 91 and 93 retain stones, whereas 92 and 94 are archaeologically located absent settings [25, p. 28]. The available source record does not resolve a finer socket- or mound-centre definition for both absent positions; we retain the reported convention.

Table 1. Provenance and boundary conventions of the dimensional inputs. Approximate readings of a published plan are distinguished from reported survey distances. Printed digits do not imply a corresponding archaeological accuracy.

Input	Value used	Measurement status	Source and feature boundary
Station short sides	91–92: 34.17 m 93–94: 32.70 m	Reported survey	Atkinson [23], reproduced by MacKie [24, p. 107]; reported centre-to-centre distances.
Station long sides	92–93: 79.93 m 91–94: 80.26 m	Reported survey	Same survey and source chain [23,24]; surviving stones and archaeologically located absent settings.
Aubrey circuit	86.44 m	Reported survey	Thom survey diameter through hole centres, tabulated by MacKie [24, p. 107].
Sarsen outer envelope; trilithon transverse span	Approximately 33.0 m; 13.7 m	Rounded plan readings	Rounded outer-face readings from Cleal et al., fold-out Plan 1 [1]; not separately published survey scalars.
Z and Y circuits	39.0 m; 54.0 m	Approximate summary	Approximate hole-centre circuit diameters reported by Cleal et al. [1, p. 260].
Sarsen inner face	97.33 ft (approximately 29.666 m)	Sensitivity only	Petrie [26, p. 23]; circle through dressed inner faces. Sensitivity only, excluded from the primary outer-envelope fit.

We fit one scale u to the mean Station short side, mean long side and Aubrey diameter, assigning exterior lengths k=(10,24,26). For measurements x_i, the through-origin least-squares estimate is $\hat{u}=\Sigma k_i x_i/\Sigma k_i^2$. The interior roles k=(4,10,12,16) then give lengths $k\hat{u}$. Signed relative residuals and their RMS measure recovery. The interior dimensions are excluded from scale estimation; their feature associations were developed with the plan available.

The Aubrey alternatives are 86.87 m from Hawkins' survey in the same MacKie table, 87.0 m in Lawson's rounded summary [25, p. 22], and 85.832 m implied by the 140.8 ft radius in MacKie's prose [24, p. 99]. The latter conflicts with that paper's appendix and is retained as an adverse source branch. The 33.0 m sarsen envelope and 13.7 m trilithon span are rounded plan readings; the 39.0 and 54.0 m hole circuits are approximate published summaries. These have coarser resolution than the Station survey. The ditch [27] and Heel Stone do not enter the calibration. S1 Note 2 retains the source ledger and alternative conventions.

Sixteen primitive Pythagorean triples with hypotenuse at most 100 define the metric comparison. On an ideal 56-position circle of diameter Φ, a chord spanning k steps is $\Phi \sin(\pi k/56)$. Combining the 16 frames with 13 unequal-leg complementary step pairs gives 208 comparisons. Sections 2.6 and 2.9 specify the comparison controls; S9.1 and S9.3 collect their extended results.

Cleal Plan 1 and the archived Rees click-plan supply separate drawing proxies for shape and directional comparisons [1] (Rees click-plan: https://timdaw37.github.io/stonehenge-plan/). The Cleal extraction uses a 20 m printed scale bar spanning 357 pixels, approximately 0.056 m per pixel; this is raster sampling, not survey accuracy. Stations 91 and 93 use projected standing-footprint centres, while 92 and 94 use socket-outline proxies, with incomplete excavation at 94. A leaning stone's footprint need not mark its original socket centre, so the alternative Station 91 placement is retained as a sensitivity branch. The Rees branch uses labels or hatch centroids for the entrance pair 1–30 and inner pairs 51–52, 53–54 and 57–58. Figure 1 distinguishes these unregistered source plans. The dimensional fit uses the separately traced measurements and rounded summaries in Table 1. S9.1 records extraction and registration comparisons.

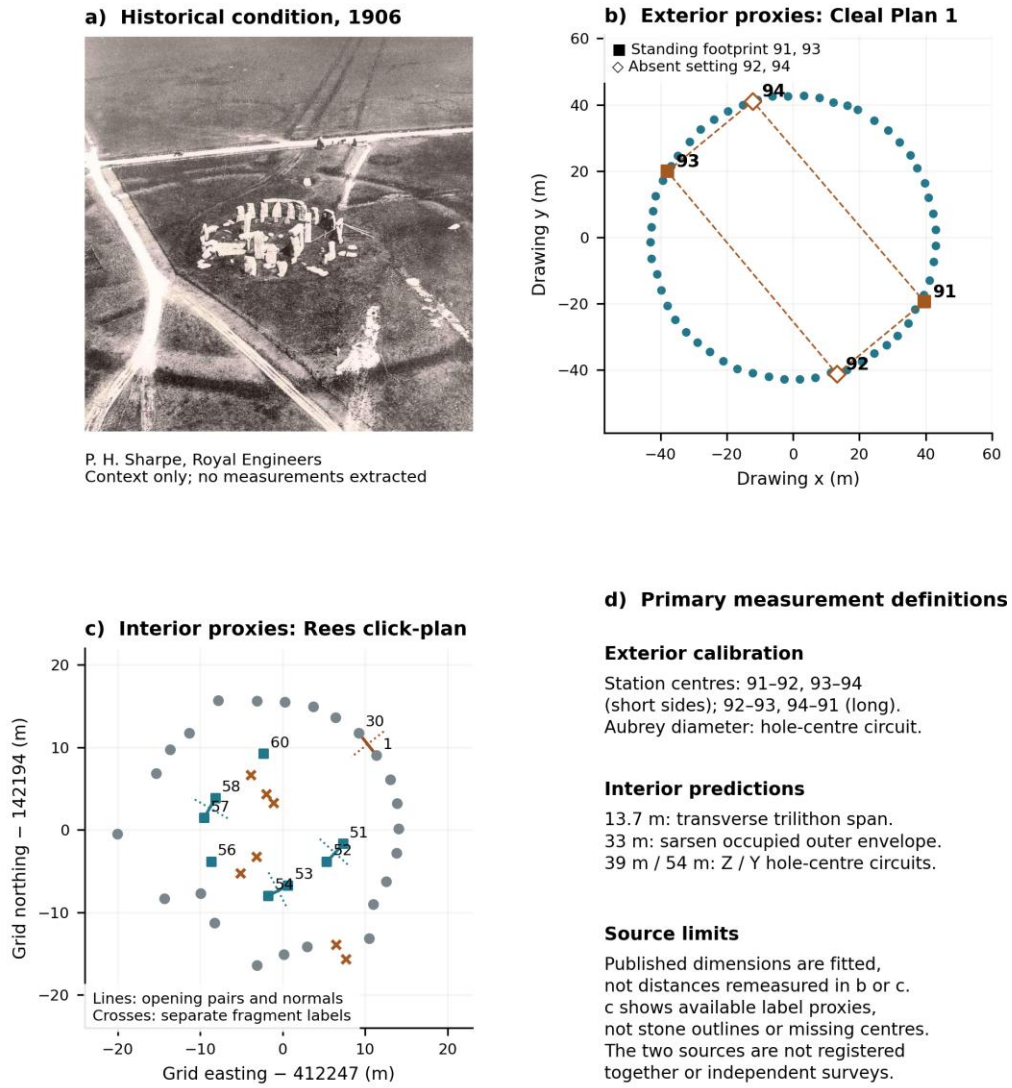


Figure 1. Archaeological setting and input definitions. (a) Philip Henry Sharpe's 1906 aerial photograph, Royal Engineers; public domain through expired Crown copyright, via Wikimedia Commons. (b) Aubrey symbols and Station proxies from Cleal Plan 1 [1]; squares mark standing footprints and diamonds absent-setting proxies. (c) Archived Rees click-plan labels and opening normals. Panels b and c use separate source coordinates. (d) Boundaries of the published dimensions used in the reconstruction. Source files and extraction code are supplied in S5.

2.2. From architectural counts to stellar fields

The map assigns each count-derived number a specific geometric role. It defines r=A−B−C, g=C, j=B+D and v=A+C−D. With q=j−g and d=v−j, the ordered list of eight numbers (the register) is Q=(r,q,d,j,d+q,v,3q,v+j), and the temporal target is W=(d,3q,r). We test this map algebraically, under exchanges of assigned geometric roles and against alternative count maps. Here r is the material radial label. The stellar counterparts of g and j are the Deneb–Sadr longitude step and Deneb–Albireo longitude span; v is the mean latitude of Deneb and Fawaris, all in the fixed J2000 ecliptic

frame. They provide a separate comparison with the stellar register and do not enter the complete field census. S9.2 gives the inverse, closure equations, historical-catalogue comparison and source definitions [28].

The main stellar census uses all 5,041 entries in the archived Hipparcos V≤6 table. A field is a five-star set generated by expanding a circular region around a catalogue star. Every catalogue entry acts as a centre, and the radius advances whenever another star enters the circle. We retain every distinct set of the five brightest enclosed stars while the centre remains in the set, with catalogue identifier breaking magnitude ties. The census is exhaustive under these circular-field and brightness rules; the following geometric selector fixes the compared roles. Constellation boundaries, timing targets, archaeological dates and horizon constraints play no role in field generation.

The minimum spanning tree is the shortest network connecting all five stars. A four-arm tree has one central star joined directly to the other four; we use that star as the hub. Otherwise we use the angular medoid, the member with the smallest total angular distance to the others. The brightest non-hub member is the first endpoint, and the remaining member most opposite in tangent bearing at the hub is the second endpoint. Their two adjacent intervals and the remaining unordered pair define the three compared intervals, called temporal channels. This selector follows section 2.9 of the related unpublished manuscript by L. G. Ribeiro and M. A. Simonssini, “Spherical certificates decouple centre and connectivity update times in evolving stellar patterns”, supplied separately for editorial assessment. Groups and roles are fixed at J2000 throughout each epoch search. Four-arm subsets are reported separately, either allowing any member to be hub or requiring the hub to be a generating cap centre. Catalogue order breaks medoid and bearing ties. The tree test requires $d(i,j)>\max[d(h,i),d(h,j)]+10^{-10}$ degree for every pair of leaves i,j; an independent Kruskal construction checks this condition.

2.3. Angular intervals and calibration

The main Hipparcos panel propagates unit directions by normalized angular proper motion from J1991.25, then applies long-term precession to the equator of date, the plane perpendicular to the modelled terrestrial rotation axis at that epoch [29–32]. HYG sensitivity panels instead normalize Cartesian p+tv from J2000, using archived distances, proper motions and radial velocities; missing radial velocities are zero. Magnitudes remain fixed. A common shift of ecliptic longitude origin cancels in longitude differences; changes of the orbital plane and stellar motion remain. The spatial module holds the J2000 ecliptic plane fixed, whereas the temporal module follows the equator of each date. Let $d_i(t)$ be the three unsigned wrapped right-ascension differences relative to the equator of date. The fixed angular model compares them with $\theta=(7°,18°,4°)$, using $R(t)=\sqrt{\{\Sigma_i[d_i(t)-\theta_i]^2/3\}}$. This corresponds to a quarter degree per count in W, the rotation angle traversed in one sidereal minute. Expressing the same calculation in sidereal minutes multiplies scores by four and leaves epochs and rankings unchanged. The quarter-degree scale is a model convention.

The free-scale comparison discards absolute angular size and tests only the proportions $w=(7,18,4)$. With $q_i(t)=d_i(t)/w_i$, define $E(t)=\mathrm{sd}(q)/\mathrm{mean}(q)$, using population standard deviation. This relative-dispersion objective vanishes when the intervals share the target proportions and is invariant to a common unit conversion. R and E answer different questions: the first tests specified angular magnitudes, while the second tests their proportions.

The radius-calibrated model expresses each interval as a fraction of its field's radius. It compares the celestial fractions d_i/ρ with the material fractions $(W_i/D)/r$, retaining the divisor D=4. For selected hub h and unit stellar directions $u_j(t)$, let $\rho(t)=\max_j \arccos[u_h(t)\cdot u_j(t)]$. We compare d_i/ρ with $\tau=W/(Dr)=(7/16,18/16,4/16)$, using $E\rho(t)=\sqrt{\{\Sigma_i[d_i(t)/\rho-\tau_i]^2/3\}}$. The reference-radius branch fixes ρ at the group-construction epoch; the dynamic branch updates it at each evaluated epoch. Angular units cancel in both branches. This replaces the fixed degree-per-count conversion with a specified correspondence between material radius, stellar extent and interval ratios, retaining the factor D.

Every complete-census objective is minimized over astronomical years −8000 to +2000 on 1-year and 0.5-year grids, with refinement of bracketed minima and endpoints. The search is independent of archaeological dates. For unit stellar directions u_i,u_j and the physical terrestrial pole k, the independent expression $\operatorname{atan2}(|k\cdot(u_i\times u_j)|,u_i\cdot u_j-(u_i\cdot k)(u_j\cdot k))$ gives the unsigned right-ascension interval. A common orthogonal basis change preserves it. No tested equatorial projection vanishes. Candidate scores and invariance results are in S8. Numerical grid agreement is not an interval certificate of global minimization.

A subsequent extension fixes the remaining pair's midpoint at −d/D, giving four non-hub positions T=(28,−72,−15,1). It fits signed right-ascension offsets with either fixed or free angular scale. The midpoint relation was selected after inspecting Cygnus; S10 provides the construction, inverse and matched tests of that choice.

2.4. Horizon and sensitivity comparisons

A stellar record made at Stonehenge requires the stars to rise above its horizon. At latitude φ=51.18° N, upper culmination is $h=90°-|\varphi-\delta|$ for stellar declination δ. The local branch requires h>0 for every member. Original fixed-scale searches and four-arm sensitivity panels reoptimize each field over all admissible epoch segments. For the complete dynamic-radius census, local first place is established by excluding every superior unrestricted candidate through feasibility checks. This latter calculation supplies a rank, without a constrained runner-up margin or feasible-field count (S8.9–S8.10).

Catalogue and state sensitivities use four nominal cap-centred four-arm panels from Hipparcos and HYG at J2000 and 3000 BCE, plus six targeted replacements of the Cygnus states in a shared HYG background. Roles, membership and tree conditions are rechecked and every retained field is refitted. These panels concern the four-arm family; the complete census uses nominal Hipparcos/J2000. S5–S9 document the source, metric-word, phase, weighting and target-order controls.

2.5. Information order and reproducibility

Information order records what was known when each comparison was specified. This is a retrospective study. S5 preserves the public Calanais metadata, extracts and checksum ledger documenting W=(28,72,16) and its nominated epoch on 26 August 2026. The Stonehenge map, feature associations and field rules were developed with relevant results available. Radius calibration followed the fixed- and free-scale comparisons; the four-position extension followed both, then its midpoint controls and material-rule census (S9.8; S10). At Woodhenge, each target entry was chosen as the closest admissible pairwise count sum or difference at the already-known date of 2600 BCE. The exhaustive target census and random-inventory comparisons followed that selection

(S11). The later operation-library comparison and deterministic measurement bounds are in S9.9. Inputs, code, candidate scores and numerical checks accompany the manuscript.

OpenAI ChatGPT assisted with literature retrieval, drafting, code construction, computational diagnostics and reproduction checks. The authors take responsibility for all generated code, its verification, source checks, numerical outputs and interpretation. S9.8, S10 and S11 record the execution history and scope of these checks.

2.6. Construction diagnostics and comparison scope

The primary dimensional reconstruction uses the following four operations. For measured short side x and long side y, let $z=\sqrt{(x^2+y^2)}$. The four dimensional operations are x, y/2, z−x and (x+y−z)/2, assigned respectively to the sarsen outer envelope, Z circuit, Y circuit and trilithon span. The ideal 10:24:26 frame gives 10u, 12u, 16u and 4u. The measured-side comparison uses the reported side means and their Euclidean diagonal without imposing that integer frame. Source-convention branches change the Aubrey input while leaving feature definitions and the fitting rule fixed. A local compression control independently multiplies each interior summary by a uniform factor in [0.8,1.2], retains the exterior scale and assigns the nearest integer multiple; 1,000,000 trials use seed 20260916. This control tests local metric compression under those rules.

A retrospective operation comparison enumerates all 212,520 ordered assignments of four distinct entries from a 23-length library, retaining the exterior-only scale. A systematic extension adds every positive difference between sides, half-sides and quarter-sides and collapses equal lengths. We derive nearest-length decision boundaries and deterministic RMS ranges for bounded input changes; these sensitivity bounds require no assumed measurement-error distribution (S9.9).

For the plan-shape comparison, each of the 14 ideal templates $k|(28-k)|k|(28-k)$, $k=1,\ldots,14$, receives one common rotation around the Aubrey centre. No Station is independently repositioned. Continuous angular gaps, assignment to numbered Aubrey positions and rotated shape fit are separate diagnostics. A freely proportioned rectangle and an ideal 5:12:13 rectangle provide comparators. The exact anchored registration fixes the Aubrey numbering rather than choosing an origin to improve the match. These operations use drawing proxies with the boundary conventions above; S9 provides the resulting residuals and sensitivity branches.

The directional construction represents a path by a cord with equal terminal tensions. The sum of its two inward-pointing terminal unit tangents defines its resultant axis. An opening normal is perpendicular to the line between its two support proxies. For unit axis u and normal n, axial similarity is $K=(u\cdot n)^2$, invariant to axis reversal. The J route is compared with the entrance normal, and V with the mean of the three individual inner-opening scores. The assigned comparison fits no rotation. Exchanging channels, changing Station 91 placement and enumerating the declared route families test this directional interpretation. Path lengths and resultant directions are separate outputs of the same construction.

For the phase comparison, the target, stellar roles, astrometry and objective remain fixed while optimization is restricted to the published archaeological intervals; minima include both boundaries and refined interior candidates. For each early-epoch channel, comparison with that channel's separately optimized Stage 2 residual establishes whether every nonnegative weighted combination favours the early epoch. Common-epoch dominance across the fixed-scale and radius objectives instead compares Cygnus at each epoch with every rival's unrestricted minimum, adding the necessary horizon restriction only to the local dynamic-radius branch.

The four-position extension fits signed offsets to $T(h)=(28,-72,h-8,h+8)$ with positive scale and a normalized residual. Its original $h=-7$ was selected from Cygnus. Matched controls either free the midpoint or let each field choose its best of the 66 specified small-integer relations. A separate material library forms every midpoint of signed pairs, with repetition, from {0,4,10,12,16,24,26}, yielding 47 distinct h values. Each rule is applied identically across fields. Exclusion witnesses establish rank lower bounds for unsuccessful rules; the surviving rule receives the full two-grid epoch search. Sections 2.7–2.8 give the remaining definitions; S10 reports the comparisons, derivations and verification outputs.

2.7. Complete-pattern loss and conditional inverse

At each epoch, wrap non-hub right-ascension offsets into $[-180°,180°)$, reflect all offsets if the first endpoint is negative, and sort the residual pair. Write the resulting vector as z. For $T(h)=(28,-72,h-8,h+8)$, the fixed-scale RMS is $R_4=\|z-T(h)/4\|/2$. The free-scale residual is $L=\|z-aT(h)\|/\|z\|$, with $a=\max(0,z\cdot T(h)/\|T(h)\|^2)$. A zero-norm vector is assigned $L=1$. The selected midpoint is $h=-7$. All fields receive the same two-grid epoch search.

The matched free-midpoint control uses $T_0=(28,-72,-8,8)$ and $e=(0,0,1,1)$, fitting $aT_0+\beta e$. Orthogonality gives $a=\max(0,z\cdot T_0/6096)$ and $\beta=(z_3+z_4)/2$; divide the residual norm by $\|z\|$. The 66-description control allows $h=\pm w_j/k$, $w=(28,72,16)$, $j=1,2,3$ and $k=2,\ldots,12$, and minimizes L over every permitted relation. Its free-midpoint lower-bound screen is 0.012239867; every retained field–template pair is optimized on both grids. For the material-rule families, adding inventory lengths, register lengths or both extends the 47-midpoint library to 73, 129 or 139 distinct values. Four previously archived valid epochs per field provide exclusion witnesses; the surviving rule receives the complete full-window census.

For the inverse, write the first two endpoint offsets as s_1 and $-s_2$, the pair midpoint as b and its width as s_3. Assuming $b=-s_1/D$ and $r=D^2$ gives $D=-s_1/b$, $K=D^2/s_3$, $C=D+(Ks_1-D^2)/2$, $B=Ks_2/3+C-D$ and $A=B+C+D^2$. The inverse is evaluated at the three archived nominal epochs and in six stellar-state variants, without refitting each variant. Nearest-integer rounding is applied only after the continuous counts have been calculated.

2.8. Structural persistence and layout-error diagnostics

For the selected trio and quintet, the outward hub tangent is $t_i=[u_i-(u_h\cdot u_i)u_h]/\|u_i-(u_h\cdot u_i)u_h\|$. The vertex-median certificate requires $G=\|\Sigma t_i\|\le 1$ and $2\Sigma d(h,i)/n+\max d(h,i)<90°$. Tree margins and role assignments are checked at each integer year from 3000 to 1500 BCE in six fixed-membership stellar scenarios. Trio shape change is $100[\max r_e/\min r_e-1]$, where $r_e=d_e(t)/d_e(J2000)$. The additional Galactic-axis diagnostic minimizes angular distance from Sgr A* to the forward Deneb–Sadr great-circle arc, separately with fixed and moving targets; it does not select roles or epochs.

The Aubrey procedure diagnostic fits a circle to all 56 numbered Cleal proxies by least-squares radial residuals. Tangential residuals are radius times the difference between unwrapped azimuth and a fitted regular 56-step sequence. Fourier contrasts remove the common phase and first harmonic associated with centre displacement. Gaussian likelihoods compare independent errors, a closed random walk, cyclic AR(1), and sector bridges with lengths 7|21|7|21 or eight sectors of seven. Bridge covariance on a sector of length m is $\min(i,j)-ij/m$; the sector origin follows the Station-derived anchor. Trace-normalized structured covariances mix with independent noise, and variance

is profiled out. AICc uses one fitted covariance parameter for independent errors and two for each other family, with the retained contrast dimension as sample size.

Sensitivity checks remove an additional harmonic, rectify the printed grid, displace the centre by 0.1, 0.25 or 0.5 m along the cardinal grid directions, and add endpoint covariance weights 0.25 or 1. Phase specificity compares all distinct integer sector shifts. Eight blocked folds with seven holes each refit covariance and trend on training data before evaluating predictive log scores. Parametric reference simulations use 2,000 draws per fitted null; click perturbations use 200 draws at halfwidths 0.5, 2, 5 and 10 pixels, with seed 20261030. All diagnostics use the drawing proxies defined in section 2.1.

2.9. Algebraic and historical comparison families

The comparisons below are sensitivity and retrospective controls of the specified models. The typed inverse of the count map is $A=(r+j+v)/2$, $B=(j+v-r-2g)/2$, $C=g$ and $D=(r+2g+j-v)/2$. Conditional uniqueness imposes $r=D^2$, $d=A/2$ and $(A-B)^2=g^2+q^2$ on strictly positive integer inventories; S9.2 gives the factorization argument. Formula controls restrict coefficients of the four counts to $-1,0,1$ and enumerate $80^4=40{,}960{,}000$ ordered maps from nonzero coefficient vectors, plus ordered count quadruples with entries $1,\ldots,60$. The stellar descriptors are the Deneb–Sadr longitude step g, Deneb–Albireo longitude span j and mean latitude v of Deneb and Fawaris, each rounded to the nearest integer before differences are formed. The historical ecliptic comparison retains the J2000 ecliptic plane when testing proper-motion stability, and separately recomputes descriptors in the ecliptic of date. These descriptors do not filter the main 19,939-field census.

The earlier regional comparison selects the five brightest stars within each of 88 IAU regions and evaluates 60 temporal role classes per region, retaining the unordered residual pair. A separate material-word library uses {4,16,28,32,40,68,72,100} to form 512 ordered triples, each with the same epoch search. Regional free-scale controls test all six permutations of 7:18:4 and relative L^1, L^2 and L^∞ losses; positivity and a common scale are retained. Two-channel ablations fit epoch and scale before reading the omitted channel. These regional families remain distinct from the circular-field census. A broader within-region census assigns all five distinct roles at $V\le5$, with $V\le4$ and $V\le6$ sensitivities, and first requires the spatial tuple. This distinct family assesses the word and chronological intervals only after fitting. The solar diagnostic compares 26 $\sin(21\pi/56)$ with obliquity expressed in degrees; that degree-identification convention is additional to the stellar model.

Geometric diagnostics compare the six great-circle distances defined by the selected trio and pair, using absolute log ratios for equal-length tests. The fixed-relation test is contrasted with the best of all 15 distance-pair equalities and with freely optimized epochs. Material shape checks enumerate 14 cyclic templates, 220 proxy triangles and the archived bounded shape–orientation family. The metric comparison includes 16 primitive Pythagorean frames with hypotenuse at most 100 and 13 complementary unequal-leg chord-step pairs. Frame perturbations multiply side measurements independently by uniform factors at ±1%, ±2% and ±5%, with 200,000 deterministic-seed trials per level.

Metric-word controls evaluate $(2z-y,3y,z-x)/u$ with $u=(10x+24y+26z)/1352$, $x=33.435$ m and $y=80.095$ m. Four Aubrey conventions supply $z=86.44,86.87,87.00$ or 85.83168 m; a fifth uses $\sqrt{(x^2+y^2)}$. Target-change bounds screen the archived regional minima before refitting every eligible class on both grids. Joint spatial–temporal comparisons fit separate positive scales to $S=(10,34,62)$ and $W=(28,72,16)$, retain both typed assignments of the final pair, and report the Pareto frontier

without a fitted weighted sum. Spatial losses are relative dispersion or minimax fractional residual; temporal loss is E.

2.10. Woodhenge comparison and target enumeration

Woodhenge's numbered rings A–F give n=(60,32,16,18,18,12), ordered outer to inner [33, Fig. 2]. The chronological benchmark is the published unitary-construction interval, 2635–2575 cal BCE (95%), modelled from rings A–C [33, pp. 14–15] (https://historicengland.org.uk/research/results/reports/94-2024). Positive pairwise sums and absolute differences from distinct ring slots generate 18 values. Their ordered Cartesian cube, allowing reuse, contains 5,832 targets. Each target divided by four is compared with the same Cygnus intervals and astrometry as in section 2.3 on both full-window grids. We count global minima within the archaeological interval, also applying the 0.2° and observed-RMS thresholds. A secondary comparison optimizes every target inside that interval. Random-inventory controls repeat the arithmetic family for 1,000 sets of six independent uniform integers in 10–60 and 1,000 sets restricted to even integers, with replacement and seed 20261030. S11.2.1 specifies these controls and replays the date-informed selection rule.

3. Results

3.1. One exterior scale recovers four interior dimensions

The frame assigns the Station rectangle's short side, long side and diagonal the ratios 5:12:13. It ranks first among the 16 primitive triples, with 1.57% side RMS compared with 6.64% for the next candidate. The combined comparison selects this frame and a 7|21|7|21 partition, first among 208 combinations: successive corners lie 7, 21, 7 and 21 equal steps apart on the ideal 56-position Aubrey circle. This discrete partition gives chords 33.08 and 79.86 m at the published Aubrey diameter, within −1.06% and −0.29% of the observed side means. Shape fits across the archived drawing conventions also select 7|21|7|21 (S9.3).

The fitted exterior scale u=3.3314 m recovers all four interior dimensions at 2.02% relative RMS (Table 2). Figure 2 presents the construction in execution order: exterior measurements, one scale, four operations and comparison with the interior. Copying the short side, halving the long side, subtracting the short side from the diagonal and constructing the inradius of the half-rectangle triangle give 10u, 12u, 16u and 4u, respectively.

Table 2. Interior dimensions recovered with the exterior-only scale. Residuals are relative to the published dimensional summaries. The same fitted u is used in every row.

Interior role	k	Observed m	Recovered m	Residual
Trilithon horseshoe span	4	13.7	13.326	-2.732%
Sarsen outer envelope	10	33.0	33.314	+0.952%
Z-hole circuit diameter	12	39.0	39.977	+2.505%
Y-hole circuit diameter	16	54.0	53.303	-1.291%

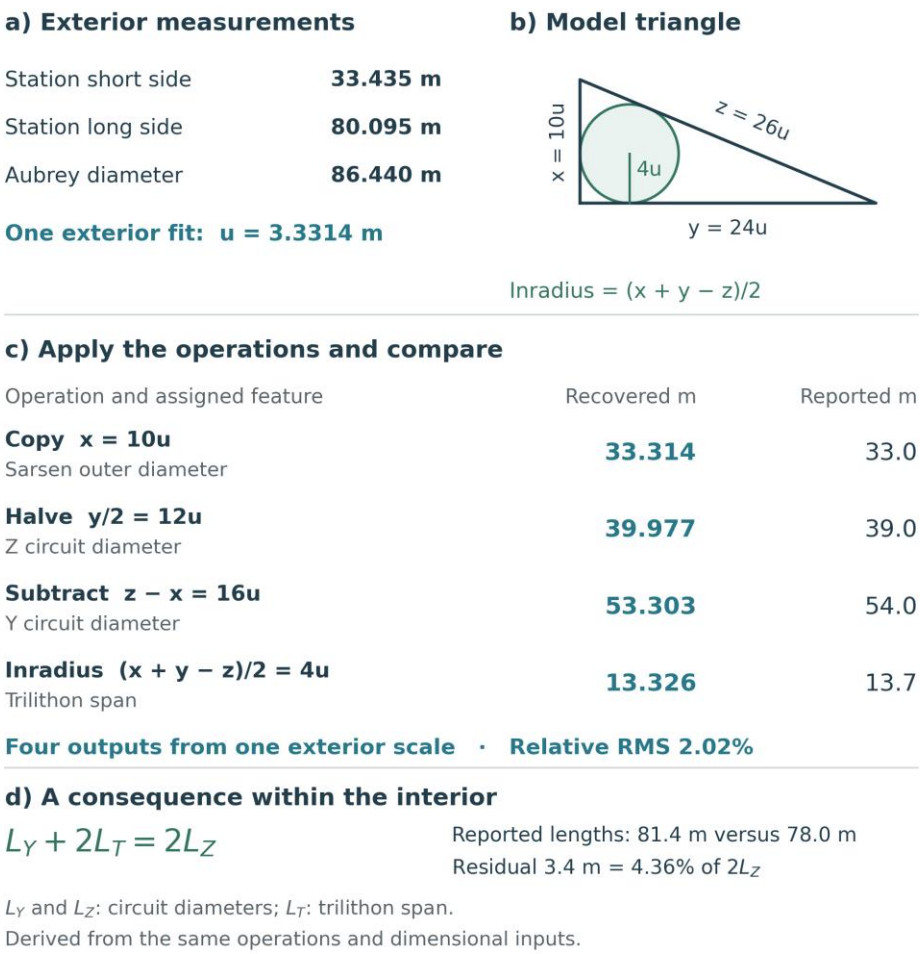


Figure 2. Construction sequence from exterior measurements to interior dimensions. (a) Reported exterior inputs determine one scale. (b) The right triangle defines the copied, halved, subtracted and inradius lengths. (c) Constructed lengths are compared with the approximate interior values in Table 1; the Station short-side mean and sarsen envelope differ by about 1.3%. (d) Eliminating the exterior lengths gives an internal consistency relation, evaluated on the same inputs. Feature assignments are retrospective; interior values do not enter the scale fit.

The transfer also works with the measured Station side means and their Euclidean diagonal: removing the imposed integer frame gives 2.014% RMS. In the local metric-compression control, 7.23% of perturbed configurations equal or improve the 2.02% recovery (median 4.12%; S8.5; S9.3).

The adopted assignment ranks first among the 212,520 alternatives: 2.01962% RMS versus 3.10002% for the next assignment. Each of its four lengths separately minimizes the corresponding absolute residual, so every positive per-feature weighting preserves the choice at the exterior calibration. The same four predictions remain first in the systematic extension to 42 distinct lengths. For stipulated independent ±1% changes to the interior summaries, the assignment remains first in both libraries while its RMS spans 1.16–2.97%. S9.9 gives the operation lists, free-scale comparisons and exact decision boundaries.

3.2. The inventory determines an ordered angular target

The architectural inventory (56,30,10,4) gives (r,g,j,v)=(16,10,34,62), q=24 and d=28. The register is Q=(16,24,28,34,52,62,72,96), and W=(28,72,16). The map has an exact typed inverse. Exchanging j and v changes the recovered Station count from 4 to 32 while leaving the other counts unchanged, giving the longitudinal–latitudinal distinction a measurable consequence within the reconstruction (Figure 3).

Three closure equations fix the entire positive integer inventory: $r=D^2$, $d=A/2$ and $p^2=g^2+q^2$, with $p=A-B$. Their unique strictly positive integer solution is (56,30,10,4), without an upper inventory bound. The same solution yields the doubled 5:12:13 frame and the target word. The temporal word alone has a one-dimensional kernel: (56+t,30,10+t,4+t), $t\geq -3$, gives the same W. The closure equations supply the additional identification, as shown by the factorization and condition-removal tests in S9.2.

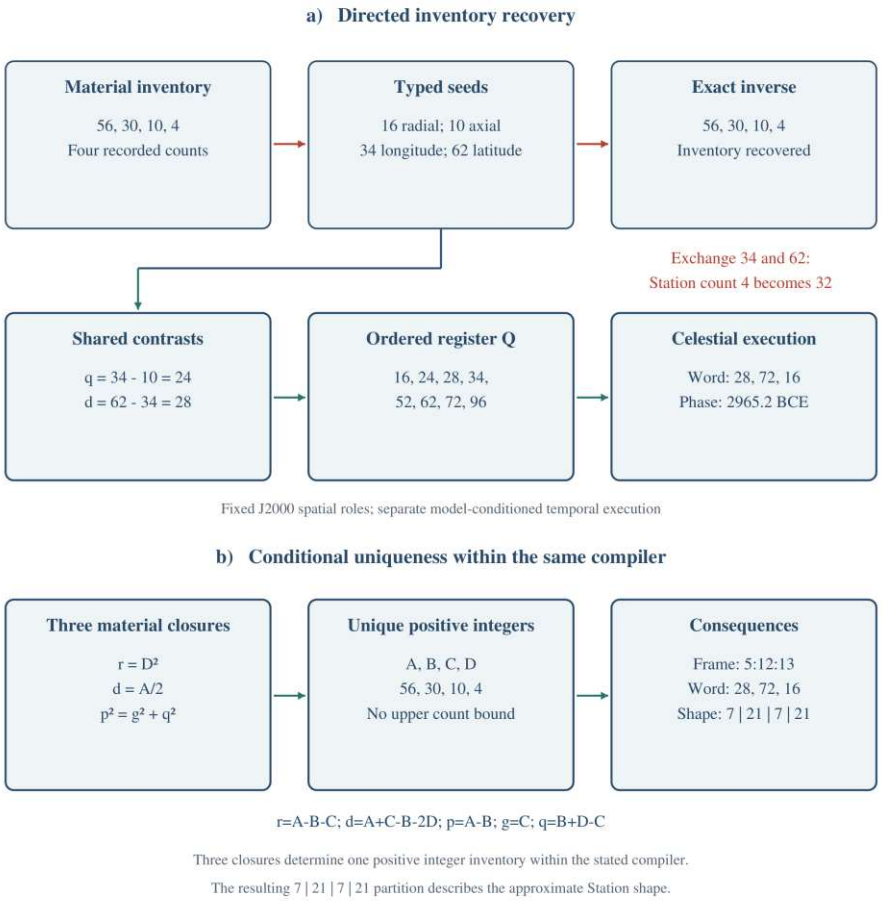


Figure 3. Ordered recovery and the inventory solution. (a) The count map and exact inverse preserve the typed roles; exchanging j and v returns 32 Station positions instead of four. (b) Solving the three stated closures gives the unique positive inventory (56,30,10,4), the doubled primitive frame and W=(28,72,16). The ecliptic comparison uses the specified J2000 frame; its coordinate sensitivity is reported in S9.2 and S9.6.

The J2000 Deneb–Sadr longitude step, Deneb–Albireo span and Deneb/Fawaris mean latitude round to (10°,34°,62°). These rounded values persist at 2965.2 BCE in that fixed plane. The ancient

ecliptic of date gives (11,35,63), while the rounded contrasts remain (24,28); S9.2 and S9.6 distinguish these constructions. In the full field analysis, the selector uses angular geometry and brightness to assign Deneb–Sadr–Albireo to the adjacent intervals and Aljanah–Fawaris to the remaining pair. Sadr is the four-arm hub. The nominal quintet remains the five-brightest set for cap radii approximately 16.239°–20.284° about Sadr. This supplies the stellar configuration used by the angular comparisons without requiring constellation boundaries (S6; S8.1). Across 9,006 sampled kinematic cases, Sadr retains both spherical-median certificates, the four-arm tree and the selected continuation (S6.4).

3.3. The complete fixed-scale census selects Cygnus

Sweeping the circular-field rule across the whole magnitude-limited catalogue generates 19,939 distinct five-star sets over 25,161 radius intervals. Cygnus ranks first under θ=(7°,18°,4°), without a four-arm entry filter or horizon restriction. Its minimum is R=0.097531516° near 2965.425 BCE. The runner-up reaches R=0.214695196° near 2430.126 BCE, an error 2.2013 times larger. That field spans the modern regions Reticulum, Hydrus and Horologium; those boundaries played no role in its generation. Table 3 compares the calibrations within their stated families. The common-catalogue intervals are (6.947°,18.151°,4.053°) at this optimum and (4.801°,12.877°,15.309°) at J2000. The resolved secondary local minimum is near 5674 BCE, with RMS 1.944°, about 19.93 times larger. Narrative_Checks in Supplementary Data 1 reproduces these illustrative values on both search grids.

The boundary-free census supersedes the earlier regional comparison based on the 88 IAU constellations, in which Cygnus also ranked first among 5,280 temporal role classes with a 1.42 runner-up error ratio (S9.5). The candidate generator and role assignment differ between panels; first place persists when constellation boundaries are removed.

Table 3. Angular calibration changes stellar selectivity. Searches span astronomical years −8000 to +2000. Error ratios compare the runner-up with Cygnus within each objective and family. The dynamic-radius horizon rank follows from unrestricted scores and feasibility; its feasible count and constrained margin were not computed. Four-position extensions and their ablations are reported in S10. Fixed R tests angular magnitudes; Free E tests proportions; Reference Eρ scales by the field radius at J2000; Dynamic Eρ updates that radius at each epoch.

Objective and family	Groups	Rank	Cygnus BCE	Error ratio
Fixed R, complete census	19,939	1	2965.4	2.201
Fixed R, necessary horizon	17,860	1	2965.4	2.626
Free E, complete census	19,939	68	2985.5	—
Free E, cap-centred four arms	256	1	2985.5	1.0155
Reference Eρ, complete census	19,939	1	2989.3	1.316
Dynamic Eρ, complete census	19,939	2	2988.0	—
Dynamic Eρ, necessary horizon	Not counted	1	2988.0	Not computed

Uniform horizon reoptimization retains Cygnus first among 17,860 fields with at least one admissible epoch, with a 2.6260 error ratio. The four-arm subsets contain 283 fields for any-member hubs and 256 for cap-centred hubs; both retain fixed-scale first place with a 12.9151 ratio. The two search grids preserve these ranks and margins (S8.9).

With absolute scale free, Cygnus reaches E=0.649026% near 2985.482 BCE and ranks 68th in the complete family. Both four-arm subsets retain first place, with a 1.0155 error ratio. The epoch moves by about 20 years. Absolute angular magnitude supplies the additional selectivity of the fixed-scale census.

The fixed-scale optimum falls within the 3000–2920 cal BCE initial-enclosure interval and the 2980–2720 cal BCE 95% ditch interval, but precedes the narrower 2940–2800 cal BCE 68% interval [2,18]. Figure 4 uses the original astrometric inputs, giving 2965.2 BCE; the common Hipparcos inputs give 2965.425 BCE under the same objective. The 0.21-year difference is far below the archaeological dating resolution. The radius and three-interval free-scale optima remain in the initial-enclosure interval, preceding the separate 95% ditch interval.

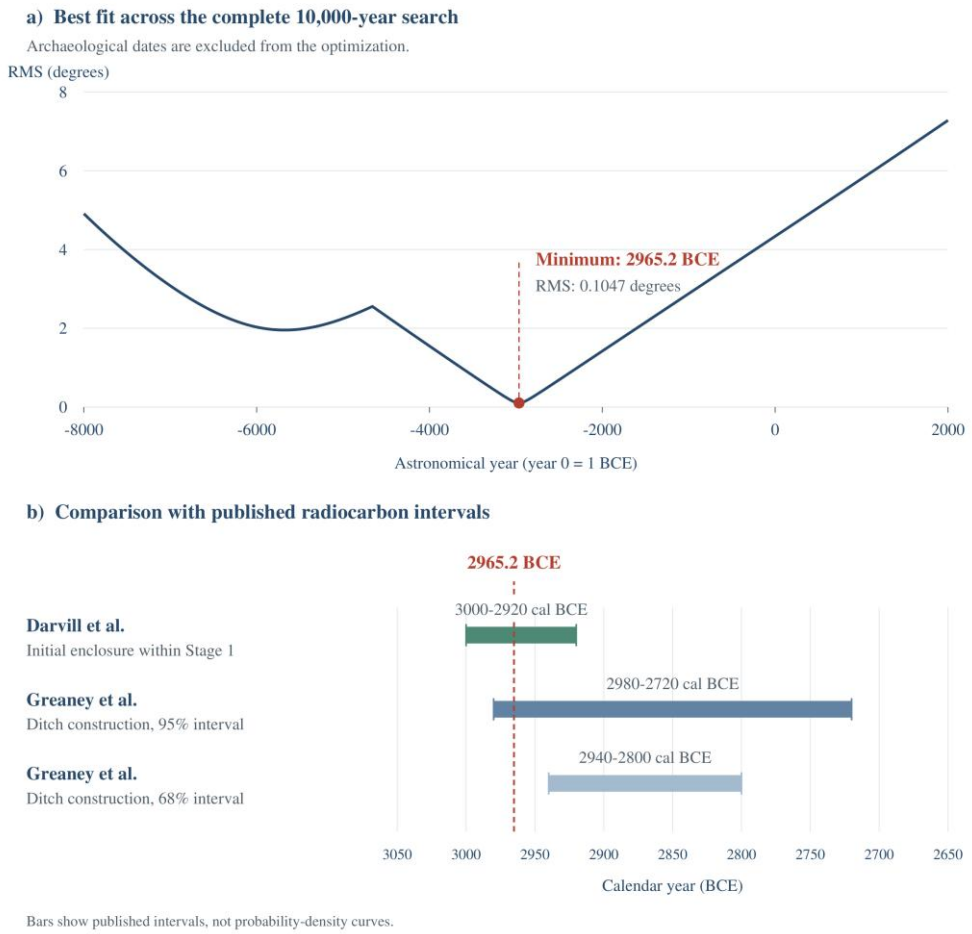


Figure 4. Astronomical optimization and archaeological chronology. (a) Full-window score for the archived primary specification, with its best-fit minimum at 2965.2 BCE. The target remains fixed while the intervals evolve. In this original specification, the resolved secondary minimum is at 5677.7 BCE, with RMS 1.956°, 18.67 times larger. (b) Comparison with the published initial-enclosure and 95% and 68% ditch intervals. Chronology is applied after optimization. The common-catalogue field census gives the closely corresponding 2965.425 BCE minimum. Bars show the published archaeological intervals.

3.4. The model favours the initial enclosure over the sarsen phase

The same angular model discriminates between Stonehenge's building phases. Its unrestricted minimum lies in the initial-enclosure interval, 3000–2920 cal BCE [2]. Restricting it to the later sarsen phase, 2620–2480 cal BCE, increases the best RMS 5.33-fold. At the early reference epoch, every channel separately improves on its own best Stage 2 residual. The early preference therefore survives every nonzero nonnegative weighting of the three channel residuals (S9.6).

3.5. The stellar radius supplies a geometric calibration

The smallest circle centred on Sadr that encloses the quintet has radius 16.239° at J2000. The material radial label is r=16; a separate ditch-centreline estimate gives 16.06–16.10u under its stated boundary convention (S9.4). Radius calibration compares fractions of these scales, with D=4 retained, rather than assigning a fixed degree per count. With ρ fixed at J2000, Cygnus is first

among all 19,939 fields: Eρ=0.006625688 near 2989.281 BCE, with a 1.3156 runner-up error ratio. With ρ updated at every epoch, it is second: Eρ=0.006154926 near 2987.992 BCE. The candidate family and role assignments are unchanged between these two tests.

The sole superior dynamic-radius field is excluded by the common necessary horizon condition throughout the search. Even its highest individual upper-culmination maximum is −14.448°, whereas all five Cygnus stars satisfy the condition at the Cygnus minimum, with the lowest upper culmination 64.772°. A restriction cannot improve any competitor's unrestricted minimum. Excluding the only superior field therefore establishes local first place for Cygnus; the complete feasibility calculations are in S8.10.

Both four-arm subsets retain first place under either radius convention, as do the four nominal catalogue/geometry panels and six targeted state scenarios. Full scores and horizon reoptimizations are in S8.10.

Across approximately 3051–2927 BCE, a common Cygnus epoch improves on every rival's separately optimized fixed-scale and reference-radius minima. Thus each rival may choose its own best epoch for each criterion and still loses both comparisons. Every nonzero nonnegative weighted sum of these two criteria, with positive normalizations, therefore selects Cygnus throughout this interval. Dynamic-radius dominance also holds under the necessary horizon condition. S8.11 gives the proof and numerical bounds.

3.6. The exterior frame also supplies directions

Two paths along the rectangle give directional predictions under equal terminal tension. J joins opposite short-side midpoints along one long edge, with length 5+24+5=34 and resultant along the short-side axis. V follows diagonal–short side–diagonal, with length 26+10+26=62 and resultant along the long-side axis. In the primary Rees proxies, the J axis is 0.45° from the entrance normal, while V has mean squared axial alignment 0.93891 with the three complete inner-opening normals. Neither comparison fits a rotation. The specified route family connects length labels and architectural directions in the same construction (Figure 5; S9.4).

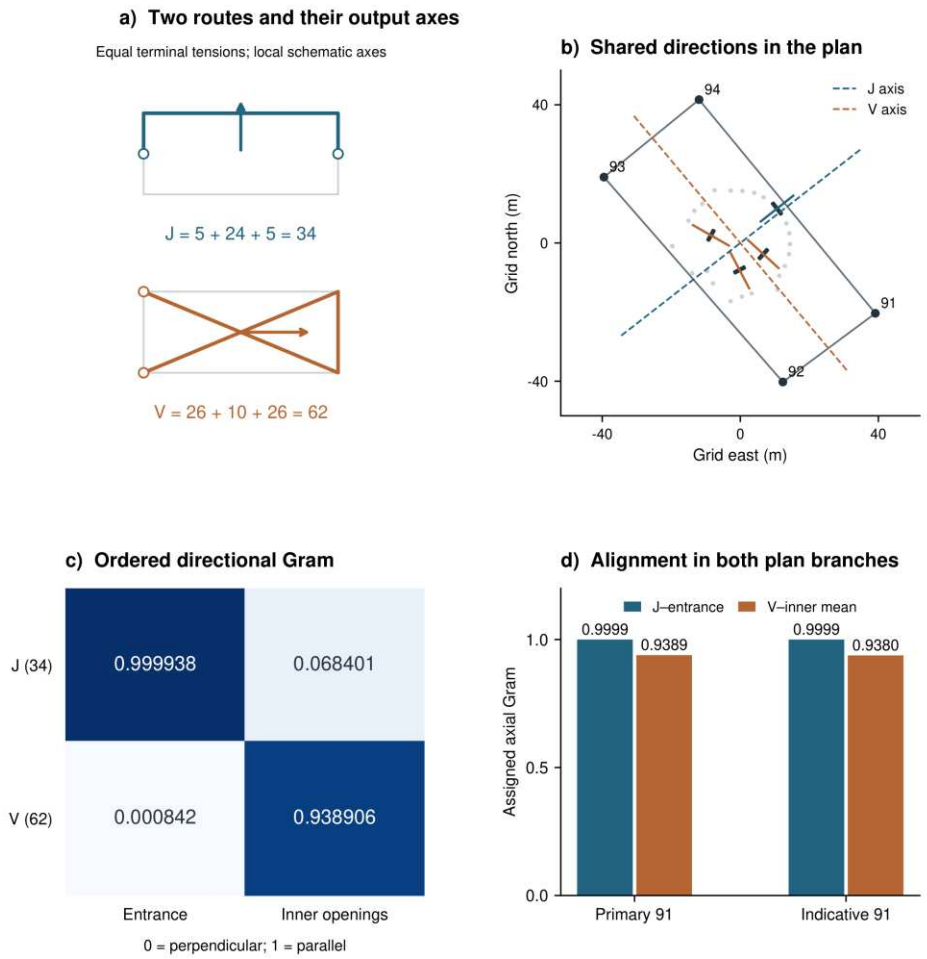


Figure 5. Outer-frame paths connect lengths with directions. (a) The J and V routes produce lengths 34 and 62 and their equal-tension axes. (b) Comparison with the entrance and inner-opening normals in the Rees grid. (c) Squared axial alignments for assigned and exchanged channels. (d) Results under both Station 91 conventions. Dashed axes show direction through the Station centroid; they do not predict force-line positions. The source-sensitive positional tests and route alternatives are retained in S9.4 and S9.6.

The positional controls distinguish these dimensional and directional results from a complete layout reconstruction. Exact Aubrey-anchored registration gives 8|21|7|20 in the primary Cleal branch, rather than the approximate 7|21|7|21 shape. Direct stellar-axis and centre-radius comparisons also fail to recover a proportional Station rectangle (S9).

3.7. Completing the pattern identifies the midpoint dependence

Adding the Cygnus-derived midpoint relation gives free-scale first place near 2976 BCE, a 2.2234 error ratio and a fitted scale of 0.2516677° per unit. Freeing that midpoint gives rank 119; allowing each field its best of 66 relation descriptions gives rank 16. In the subsequent material-rule test, only one of 47 construction-derived midpoints, −7, retains first place. These matched comparisons identify the specific relation responsible for the complete-pattern result (S10.3, S10.7).

The midpoint relation and $r=D^2$ also give an inverse independent of angular units. At the fitted epoch it rounds to (56,30,10,4), including across six alternative Cygnus states. S10.4 gives the algebra,

continuous counts and epoch sensitivity. This closes the model under its added relation; the original three-interval census is unchanged.

3.8. A Woodhenge target matches its timber-construction interval

The Woodhenge extraction ($n_1-n_2, n_1+n_6, n_2-n_6$) gives (28,72,20), whose full-window minimum is near 2609 BCE with RMS 0.169091°. It falls within the published 2635–2575 cal BCE construction interval [33]. Between the Stonehenge and Woodhenge optima, the third celestial interval increases by 0.835°, while the first two change by −0.137° and −0.344°. The change from 16 to 20 in the third target entry follows the largest coordinate change in the astronomical model (S11.3). Figure 6 combines this chronological comparison with the complete field selection.

Of the 5,832 targets, 33 have global minima in the archaeological interval; only (28,72,20) also has RMS below 0.2°, or no greater than its observed error. It ranks sixth by RMS across all epochs. Optimizing every target inside the archaeological interval gives a next-best error of 0.416338°, 2.46 times larger. Both grids preserve these counts. The joint interval-and-observed-error criterion is met by 33/1,000 random uniform inventories (3.3%) and 105/1,000 all-even inventories (10.5%); 917/1,000 uniform inventories attain RMS below 0.2° somewhere in the full time window. These controls quantify the contribution of the chronological condition and its sensitivity to the reference distribution (S11.2.1).

The separate retrospective transcription in S11.4 maps B=30, r=16 and q=24 to all six Woodhenge counts and inverts to the Stonehenge 10:24:26 frame and inventory (56,30,10,4).

4. Discussion

One exterior frame organizes four interior dimensions across Stonehenge's building sequence. The construction reaches 2.02% RMS, and using the measured sides without the exact integer frame preserves the agreement. Figure 2 makes the procedure reproducible from its source measurements to its outputs.

Eliminating the exterior lengths gives a relation within the interior. For circuit diameters $L_Z=y/2$ and $L_Y=z-x$ and trilithon span $L_T=(x+y-z)/2$, the construction requires $L_Y+2L_T=2L_Z$, independently of the fitted scale and exact integer proportions. The approximate Table 2 values give 81.4 m versus 78.0 m: a 3.4 m discrepancy, or 4.36% relative to $2L_Z$. This is a consistency check derived from the same operations and dimensional inputs. Construction_Sequence in Supplementary Data 1 reproduces the calculation and Figure 2.

For an incomplete monument, the equations identify which exterior measurements constrain each interior dimension and which proposed interior revisions remain mutually consistent. For example, holding the Z-circuit diameter fixed, increasing a proposed Y-circuit diameter by 1 m requires reducing the trilithon span by 0.5 m under the construction. The transmission hypothesis requires lengths to track x, y/2, z−x and (x+y−z)/2, including departures from ideal proportions and using the same feature boundaries across phases. A dimensional discrepancy identifies where that proposed shared design fails.

The operation comparison also identifies measurements that can change the reconstruction. At the current exterior calibration, a sarsen outer diameter below 32.48 m or a Y-circuit diameter above 54.97 m selects a competing length in the expanded library. These boundaries make the boundary

conventions in Table 1 consequential: a refined survey can test the dimensional assignments directly. S9.9 specifies the tolerance within which each assignment is stable.

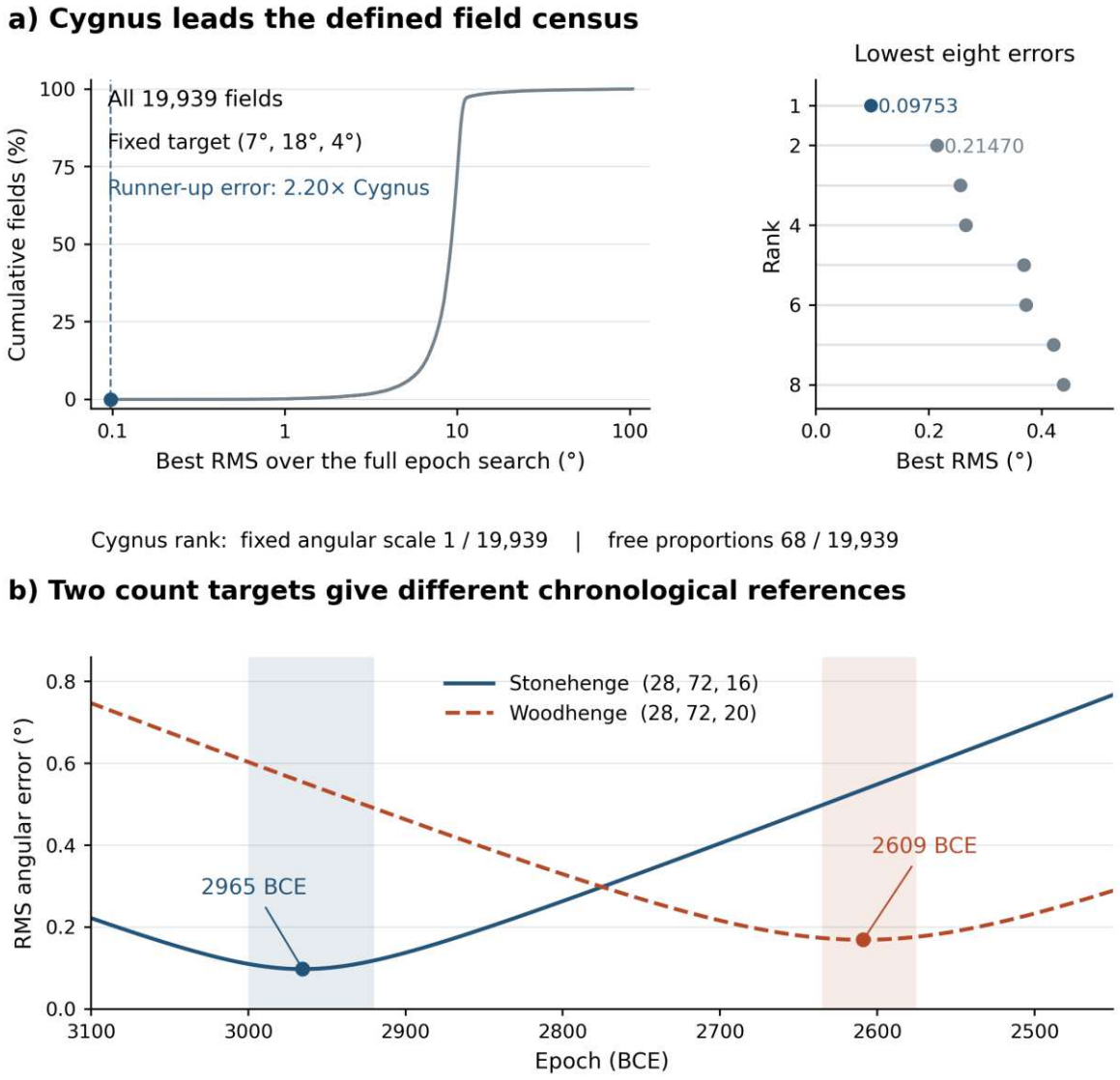


Figure 6. Field selection and chronological references. (a) Cumulative distribution of the best fixed-scale RMS for all 19,939 fields under the stated generation and role rules. Each field is optimized over the full epoch window. The right-hand enlargement shows the eight lowest errors; Cygnus is blue. The separate rank comparison reports the free-proportion sensitivity. (b) Cygnus RMS for the Stonehenge and Woodhenge targets, using the same catalogue and angular calibration. Shading marks the published construction intervals, 3000–2920 cal BCE [2] and 2635–2575 cal BCE [33]; points mark the full-window minima. Woodhenge target selection used its known chronology (Methods 2.5).

The archaeological sequence gives these relations their historical significance. The Aubrey circuit belongs to the early enclosure; the major sarsen settings and possibly the Stations are assigned to Stage 2, 2620–2480 cal BCE, while Y/Z excavation is later, 1630–1520 cal BCE [2]. Station dating remains insecure [1–3], and heritage summaries distinguish the central stones near 2500 BCE from

the later holes (https://www.english-heritage.org.uk/visit/places/stonehenge/history-and-stories/history/). Historical use of one dimensional rule entails reuse or transmission across these episodes. The inventory combines 56 early Aubrey positions with 30 sarsen and 10 trilithon uprights and four Stations, yet its best-fit celestial reference falls in the initial-enclosure interval. Every temporal channel fits that early epoch better than any epoch in the later sarsen interval. The model places the combined inventory's best-fit stellar reference in the earlier phase.

Centres and socket positions supply distinct tests of transmission. Reuse of the Aubrey centre requires agreement between independently fitted phase-specific centres within positional uncertainties. Inheritance of a complete socket pattern requires a placement algorithm in addition to the four dimensional equations. A displaced centre challenges centre reuse; failure of the dimensional relations challenges the construction itself. These tests distinguish the parts of a proposed design that persisted through rebuilding.

The count map specifies the target intervals; precession and stellar motion locate their best stellar matches in time. Those reference epochs can then be compared with dated building phases. Cygnus ranks first in the fixed-scale census and under reference-radius calibration; over a common early interval it beats every rival's separately optimized minimum in both criteria. Selection survives any nonzero nonnegative weighting of those two calibrated objectives. The phase comparison distinguishes initial enclosure from later stone setting. These results add a specified construction and stellar reference to solar, lunar, depositional and landscape interpretations [5–8,34–41] and the funerary evidence [42]. At the common-catalogue optimum, the five upper-culmination altitudes range from 64.75° to 80.63°, with Deneb at 75.07° and Sadr at 72.76°: the configuration was high above Stonehenge's horizon at transit.

Woodhenge extends the comparison across sites and construction dates. Holding the astronomy and calibration fixed, its count target moves the optimum into the later timber-construction interval. The material transcription separately connects all six ring counts with the Stonehenge inventory. The regional question is now explicit: whether related construction rules carried both dimensional information and a celestial reference through rebuilding. Testing that regional hypothesis requires applying a fixed extraction rule to further monuments. Section 2.5 records the date-informed Woodhenge selection.

Recent evidence for the distant origins of Stonehenge's stones documents long-range material connections [43]. The present reconstruction specifies operations and a stellar reference to investigate alongside those material connections: the relations linking the exterior frame to interior dimensions and the count-derived intervals. Each proposed link has a traceable input, boundary convention and numerical consequence, allowing competing reconstructions of the incomplete monument to be compared on the same terms.

Historical attribution is the archaeological inference still to test. Section 2.5 documents the retrospective choices of count map, feature associations and stellar target. Ranks and random-inventory frequencies describe specified comparison families; they are not probabilities of prehistoric intention or corrections for the full research search history. Table 3 and section 3.7 identify the calibration and midpoint dependencies. The common-epoch dominance interval is a model comparison, not a construction-date confidence interval.

Rounded interior summaries and digitized plans limit positional inference; an independent georeferenced Station–Aubrey survey was unavailable. Exact registration and the Aubrey residual test do not identify a unique setting-out procedure (S9.6; S10.5). Catalogue/state sensitivities cover

the four-arm family, while the full census uses nominal Hipparcos/J2000. These boundaries specify the scope of the present reconstruction.

The equations give the next archaeological observations a defined purpose. Independent exterior and interior measurements test propagation of non-ideal geometry. Dated traces of repeated setting-out operations test persistence across phases. An unused stellar observable can distinguish Cygnus from competing complete models under the same archaeological constraints. These are direct tests of the relations established here.

The reconstruction connects Stonehenge's exterior geometry, interior dimensions and a celestial reference near its initial enclosure. Woodhenge adds a later chronological concordance and a relation between the two inventories. For heritage science, the equations make competing reconstructions of an incomplete, repeatedly rebuilt monument directly comparable: a revised dimension carries explicit consequences for the others. The count models supply temporal references for comparison with the archaeological sequence.

Supplementary materials

Supplementary Information is supplied as one PDF, containing extended architectural results (S9), geometric certificates and comparisons (S6–S8), complete-pattern results and derivations (S10), and the Woodhenge comparison (S11). Supplementary Data 1 contains the executable code, numerical inputs, candidate tables and preserved research records S1–S11, with a module index and checksums. The operational definitions are in main Methods; archived versions remain identified as historical records. The bibliography below is shared with the current Supplementary Information. Its navigation index maps earlier section and reference numbers.

Author Contributions

Conceptualization, L.G.R. and M.A.S.; methodology, L.G.R.; investigation, L.G.R.; formal analysis, L.G.R.; validation, M.A.S.; visualization, L.G.R.; writing—original draft preparation, L.G.R.; writing—review and editing, L.G.R. and M.A.S.

Data availability

Numerical inputs, complete candidate outputs, archived plan proxies, figure sources and analysis code are supplied in Supplementary Data 1 (modules S1–S11), supporting reproducible reuse [44]. The prior grammar and temporal operator are documented in public deposits (https://zenodo.org/records/22103786; https://zenodo.org/records/22691368); the S5 archive records their provenance. S2 contains the shared Hipparcos table; S6–S8 include their catalogue extracts, states and reproduction dependencies, with the HYG licence retained. The third-party Rees raster used in one S3 diagnostic is obtained from its source (https://timdaw37.github.io/stonehenge-plan/); S3 records its expected hash. The S6–S8, S10 and S11 numerical calculations require no external data download after installation of the declared Python dependencies. S11 provides the random-inventory outputs, transcribed Woodhenge ring inventory and the provenance of the published chronological interval [33].

Code availability

Analysis code, input tables, candidate outputs, dependency specifications and reproduction instructions are supplied in Supplementary Data 1. Its README maps the S2–S8, S10 and S11

modules, preserved source archives and checksums. S10_Material_Rules/README.txt specifies regeneration of the omitted intermediate score array and cache before the full verifier is run. S9.8 and the versioned verification files document the execution history, environments and checks. Narrative_Checks reproduces the explanatory interval, local-minimum and culmination values from the archived astrometric inputs. S11_Woodhenge/README.txt identifies the target census, random-inventory controls, material transcription, conditional integer decoder and retained geometric controls. Construction_Sequence reproduces Figure 2 and verifies the derived interior relation. Construction_Alternatives supplies the complete 23-operation enumeration, systematic difference extension and measurement decision bounds. Figure6_Sky_Comparison reproduces Figure 6 from the archived census and S11 model.

Acknowledgments

This research received no external funding. The authors thank the Ágora Study Group for sustained discussion and independent study support.

Competing Interests

The authors declare no competing interests.

References

1. Cleal, R. M. J., Walker, K. E. & Montague, R. Stonehenge in its landscape: twentieth-century excavations. English Heritage Archaeological Report 10; 1995.

2. Darvill, T., Marshall, P., Parker Pearson, M. & Wainwright, G. Stonehenge remodelled. *Antiquity* **86,** 1021–1040 (2012). https://doi.org/10.1017/S0003598X00048225

3. Parker Pearson, M. et al. The age of Stonehenge. *Antiquity* **81,** 617–639 (2007). https://doi.org/10.1017/S0003598X00095624

4. Abbott, M. & Anderson-Whymark, H. Stonehenge laser scan: archaeological analysis report. English Heritage Research Report Series 32/2012; 2012.

5. Darvill, T. Keeping time at Stonehenge. *Antiquity* **96,** 319–335 (2022). https://doi.org/10.15184/aqy.2022.5

6. Hawkins, G. S. Stonehenge decoded. New York: Doubleday; 1965.

7. Thom, A. Megalithic sites in Britain. Oxford: Oxford University Press; 1967.

8. Ruggles, C. L. N. Astronomy in prehistoric Britain and Ireland. New Haven: Yale University Press; 1999.

9. Snoeck, C. et al. Strontium isotope analysis on cremated human remains from Stonehenge support links with west Wales. *Sci. Rep* **8,** 10790 (2018). https://doi.org/10.1038/s41598-018-28969-8

10. Parker Pearson, M. et al. Megalith quarries for Stonehenge's bluestones. *Antiquity* **93,** 45–62 (2019). https://doi.org/10.15184/aqy.2018.111

11. Madgwick, R. et al. Multi-isotope analysis reveals that feasts in the Stonehenge environs and across Wessex drew people and animals from throughout Britain. *Sci. Adv* **5,** eaau6078 (2019). https://doi.org/10.1126/sciadv.aau6078

12. Nash, D. J. et al. Origins of the sarsen megaliths at Stonehenge. *Sci. Adv* **6,** eabc0133 (2020). https://doi.org/10.1126/sciadv.abc0133

13. Gaffney, V. et al. A massive late Neolithic pit structure associated with Durrington Walls henge. *Internet Archaeol* **55** (2020). https://doi.org/10.11141/ia.55.4

14. Parker Pearson, M. et al. The original Stonehenge? A dismantled stone circle in the Preseli Hills of west Wales. *Antiquity* **95,** 85–103 (2021). https://doi.org/10.15184/aqy.2020.239

15. Nash, D. J. et al. Petrological and geochemical characterisation of the sarsen stones at Stonehenge. *PLoS ONE* **16,** e0254760 (2021). https://doi.org/10.1371/journal.pone.0254760

16. Ciborowski, T. J. R. et al. Local and exotic sources of sarsen debitage at Stonehenge revealed by geochemical provenancing. *J. Archaeol. Sci. Rep* **53,** 104406 (2024). https://doi.org/10.1016/j.jasrep.2024.104406

17. Clarke, A. J. I. et al. A Scottish provenance for the Altar Stone of Stonehenge. *Nature* **632,** 570–575 (2024). https://doi.org/10.1038/s41586-024-07652-1

18. Greaney, S., Hajdas, I., Dee, M. & Marshall, P. Beginning of the circle? Revised chronologies for Flagstones and Alington Avenue, Dorchester, Dorset. *Antiquity* **99,** 655–671 (2025). https://doi.org/10.15184/aqy.2025.28

19. Gaffney, V. et al. The perils of pits: further research at Durrington Walls henge, 2021–2025. *Internet Archaeol* **69** (2025). https://doi.org/10.11141/ia.69.19

20. De Smedt, P. et al. Novel insights into prehistoric land use at Stonehenge by combining electromagnetic and invasive methods with a semi-automated interpretation scheme. *J. Archaeol. Sci* **143,** 105557 (2022). https://doi.org/10.1016/j.jas.2022.105557

21. Liu, X. et al. Using Source Feature Matrix for interpreting the result in virtual reconstruction of cultural heritage sites. *npj Herit. Sci* **13,** 83 (2025). https://doi.org/10.1038/s40494-025-01658-2

22. Ribeiro, L. G. & Simonssini, M. A. The hidden code of Cygnus [O Código Oculto de Cygnus] (2026; in Portuguese). ISBN 978-65-266-6755-2.

23. Atkinson, R. J. C. Some new measurements on Stonehenge. *Nature* **275,** 50–52 (1978). https://doi.org/10.1038/275050a0

24. MacKie, E. A new look at the astronomy and geometry of Stonehenge. *Cult. Cosmos* **16,** 89–107 (2012).

25. Lawson, A. J. The structural history of Stonehenge. *Proc. Br. Acad* **92,** 15–37 (1997).

26. Petrie, W. M. F. Stonehenge: plans, description, and theories. London: Edward Stanford; 1880.

27. Field, D. & Pearson, T. Stonehenge landscape: an archaeological analysis of the field survey. English Heritage Research Department Report Series 109-2010; 2010.

28. Verbunt, F. & van Gent, R. H. The star catalogues of Ptolemaios and Ulugh Beg: machine-readable versions and comparison with the modern Hipparcos catalogue. *Astron. Astrophys* **544,** A31 (2012). https://doi.org/10.1051/0004-6361/201219596

29. van Leeuwen, F. Validation of the new Hipparcos reduction. *Astron. Astrophys* **474,** 653–664 (2007). https://doi.org/10.1051/0004-6361:20078357

30. Vondrák, J., Capitaine, N. & Wallace, P. New precession expressions, valid for long time intervals. *Astron. Astrophys* **534,** A22 (2011). https://doi.org/10.1051/0004-6361/201117274

31. Vondrák, J., Capitaine, N. & Wallace, P. New precession expressions, valid for long time intervals (corrigendum). *Astron. Astrophys* **541,** C1 (2012). https://doi.org/10.1051/0004-6361/201117274e

32. Wenger, M. et al. The SIMBAD astronomical database. *Astron. Astrophys. Suppl. Ser* **143,** 9–22 (2000). https://doi.org/10.1051/aas:2000332

726 33. Marshall, P., Chadburn, A., Hajdas, I., Dee, M. & Pollard, J. Woodhenge, Durrington, Wiltshire:
727 radiocarbon dating and chronological modelling. Historic England Research Report Series 94/2024
728 (2024).
729 34. Pollard, J. & Ruggles, C. Shifting perceptions: spatial order, cosmology, and patterns of
730 deposition at Stonehenge. Camb. Archaeol. J 11, 69–90 (2001).
731 https://doi.org/10.1017/S095977430100004X
732 35. Ruggles, C. & Chadburn, A. Missing data. Cosmovisiones/Cosmovisões 5(1), 99–109 (2024).
733 https://doi.org/10.24215/26840162e007
734 36. Magli, G. & Belmonte, J. A. Archaeoastronomy and the alleged ‘Stonehenge calendar’. Antiquity
735 97, 745–751 (2023). https://doi.org/10.15184/aqy.2023.33
736 37. Darvill, T. Times they are a-changin’: a response to Magli and Belmonte. Antiquity 97, 752–754
737 (2023). https://doi.org/10.15184/aqy.2023.61
738 38. Hoyle, F. Stonehenge—an eclipse predictor. Nature 211, 454–456 (1966).
739 https://doi.org/10.1038/211454a0
740 39. Atkinson, R. J. C. Moonshine on Stonehenge. Antiquity 40, 212–216 (1966).
741 https://doi.org/10.1017/S0003598X0003252X
742 40. Magli, G. Archaeoastronomy of the Temples of the Bekaa Valley. Heritage 4, 1526–1537 (2021).
743 https://doi.org/10.3390/heritage4030084
744 41. Magli, G. The 1 April 2471 b.C. Eclipse and the End of the Fourth Egyptian Dynasty. Heritage 8,
745 492 (2025). https://doi.org/10.3390/heritage8110492
746 42. Willis, C. et al. The dead of Stonehenge. Antiquity 90, 337–356 (2016).
747 https://doi.org/10.15184/aqy.2016.26
748 43. Parker Pearson, M. et al. Stonehenge and its Altar Stone: the significance of distant stone
749 sources. Archaeology International 27, 113–137 (2024). https://doi.org/10.14324/AI.27.1.13
750 44. Richards, J. & Brimblecombe, P. The transfer of heritage modelling from research to practice.
751 Herit. Sci 10, 17 (2022). https://doi.org/10.1186/s40494-022-00650-4
752 45. Laskar, J. Secular terms of classical planetary theories using the results of general theory.
753 Astron. Astrophys 157, 59–70 (1986).

Supplementary Files

This is a list of supplementary files associated with this preprint. Click to download.

- SupplementaryData1CodeandData.zip
- SupplementaryInformationv156.pdf